remote sensing

MDPI

Article

Estimation of Rice Growth Parameters Based on Linear Mixed-Effect Model Using Multispectral Images from Fixed-Wing Unmanned Aerial Vehicles

Yanyu Wang [1,2,3,4], Ke Zhang [1,2,3,4], Chunlan Tang [1,2,3,4], Qiang Cao [1,2,3,4], Yongchao Tian [1,2,3,4], Yan Zhu [1,2,3,4], Weixing Cao [1,2,3,4] and Xiaojun Liu [1,2,3,4,*]

1 National Engineering and Technology Center for Information Agriculture, Nanjing Agricultural University, Nanjing 210095, China; 2017801189@njau.edu.cn (Y.W.); 2017201080@njau.edu.cn (K.Z.); 2018801203@njau.edu.cn (C.T.); qiangcao@njau.edu.cn (Q.C.); yctian@njau.edu.cn (Y.T.); yanzhu@njau.edu.cn (Y.Z.); caow@njau.edu.cn (W.C.)
2 Key Laboratory for Crop System Analysis and Decision Making, Ministry of Agriculture and Rural Affairs, Nanjing Agricultural University, Nanjing 210095, China
3 Jiangsu Key Laboratory for Information Agriculture, Nanjing Agricultural University, Nanjing 210095, China
4 Jiangsu Collaborative Innovation Center for Modern Crop Production, Nanjing Agricultural University, Nanjing 210095, China
* Correspondence: liuxj@njau.edu.cn; Tel.: +86-25-84396804; Fax: +86-25-84396672

Received: 19 May 2019; Accepted: 4 June 2019; Published: 8 June 2019

Abstract: The accurate estimation of aboveground biomass (AGB) and leaf area index (LAI) is critical to characterize crop growth status and predict grain yield. Unmanned aerial vehicle (UAV) -based remote sensing has attracted significant interest due to its high flexibility and easiness of operation. The mixed effect model introduced in this study can capture secondary factors that cannot be captured by standard empirical relationships. The objective of this study was to explore the potential benefit of using a linear mixed-effect (LME) model and multispectral images from a fixed-wing UAV to estimate both AGB and LAI of rice. Field experiments were conducted over two consecutive years (2017–2018), that involved different N rates, planting patterns and rice cultivars. Images were collected by a compact multispectral camera mounted on a fixed-wing UAV during key rice growth stages. LME, simple regression (SR), artificial neural networks (ANN) and random forests (RF) models were developed relating growth parameters (AGB and LAI) to spectral information. Cultivar (C), growth stage (S) and planting pattern (P) were selected as candidates of random effects for the LME models due to their significant effects on rice growth. Compared to other regression models (SR, ANN and RF), the LME model improved the AGB estimation accuracy for all stage groups to varying degrees: the R^2 increased by 0.14–0.35 and the RMSE decreased by 0.88–1.80 t ha^{-1} for the whole season, the R^2 increased by 0.07–0.15 and the RMSE decreased by 0.31–0.61 t ha^{-1} for pre-heading stages and the R^2 increased by 0.21–0.53 and the RMSE decreased by 0.72–1.52 t ha^{-1} for post-heading stages. Further analysis suggested that the LME model also successfully predicted within the groups when the number of groups was suitable. More importantly, depending on the availability of C, S, P or combinations thereof, mixed effects could lead to an outperformance of baseline retrieval methods (SR, ANN or RF) due to the inclusion of secondary effects. Satisfactory results were also obtained for the LAI estimation while the superiority of the LME model was not as significant as that for AGB estimation. This study demonstrates that the LME model could accurately estimate rice AGB and LAI and fixed-wing UAVs are promising for the monitoring of the crop growth status over large-scale farmland.

Keywords: aboveground biomass; leaf area index; vegetation index; linear mixed-effect model; UAV multispectral image; remote sensing; rice

1. Introduction

Monitoring crop growth status efficiently and in a non-destructive way is necessary for precision crop management [1]. Aboveground biomass (AGB) and leaf area index (LAI) are important growth parameters with which to evaluate crop growth status [2,3]. Both have been applied to describe the canopy structure of plants and to predict grain yield [4]. In addition, AGB and LAI have been reported to affect the global carbon cycle and climate change [5,6]. It is therefore critical to efficiently and rapidly measure crop AGB and LAI.

As a developing approach, remote sensing technology has been successfully used for crop growth monitoring in recent decades [1,7,8]; examples are its use as a satellite-based platform, manned airborne platform and in ground-based spectral devices. However, several limitations still apply for these platforms. Satellite-based platforms are restrained by deficient spatio-temporal resolution and cloud cover, manned airborne platforms have relatively high operating costs and ground-based spectral devices are laborious and suffer from inefficient operation [9–11]. In comparison, rapid-developed unmanned aerial vehicle (UAV) platforms provide an economical and high-efficiency approach to meet the continuously growing demands for improved spatial, temporal and spectral resolutions [10–12].

Among UAV-based crop monitoring studies, sensors have typically been multispectral and hyperspectral cameras that target biomass estimation, LAI monitoring or grain yield prediction [1,13,14]. In recent years, UAV-based multispectral images were used to estimate the rice growth status and predict grain yield. For example, Devia et al. used seven vegetation indices, combined with multivariable regressions to monitor agronomy parameters at different rice growth stages [15]. Duan et al. integrated UAV-based vegetation indices (VIs) and abundance information obtained from spectral mixture analysis to improve the prediction accuracy of rice yield at the heading stage [16]. In addition, most UAV-based studies used multi-rotor UAVs due to their high stability, superior image quality and good controllability. However, many multi-rotor UAVs do not meet the requirements of large-scale crop monitoring with regard to flight speeds and flight duration [10]. In contrast, most fixed-wing UAVs can fly at high speeds and usually have a long flight duration; however, the flight speeds are too fast to capture high-quality images and the operation is more complicated than that of multi-rotor UAVs [17]. As a result, little attention has been directed to fixed-wing UAVs in the field of crop monitoring.

In addition to different remote sensing platforms, scholars have also used various retrieval methods to quantitatively retrieve crop growth parameters [18–20]. These methods can generally be divided into two categories: empirical and physical [21]. With advantages of higher computational efficiency and lower instrumental requirements, empirical methods have been more widely applied than physical methods [21]. Furthermore, although empirical methods are commonly established via parametric regression, non-parametric regression is used more frequently, such as artificial neural network (ANN) and random forest (RF) regression models. ANN regression models have been successfully applied to estimate crop properties, such as crop biomass [18], LAI [19] and foliage nitrogen concentrations [22]. A range of studies used the RF regression model to map crop attributes, for example, biomass retrieval [23], LAI retrieval [24] and nitrogen status monitoring [25].

While empirical methods have been widely applied and extended, the empirical regression relationship still cannot control deviation from many secondary experimental factors and its parameters are condition specific [26–28]. A review by Corti et al. indicated that the factors (e.g., crop growth stage, sensor type, acquisition mode, sensed target and spatial resolution) exert different effects on the performance of maize variables estimation; furthermore, the estimation models have different forms and performance in response to different factors [26]. Kang et al. also suggested that the relationship between LAI and VI is not unique, especially in the agricultural setting but rather represented by a family of equations as a function of the specific geographical, biological and environmental setting [27]. In addition, other plant-related factors were found to affect canopy reflectance (e.g., plant species, development stage, age and site); however, the empirical regressions did not take these factors into account [28,29]. These issues have been identified as major limitation for the wide application of the empirical method. A powerful approach is needed to generalize empirical relationships to fit global samples across different crop types and growth stages.

The mixed-effect model might provide new insights for the development of universal models for crop growth parameters estimation. The mixed-effect model can quantify the relationships between explanatory variables and response variables by breaking down the regression into both fixed effects and random effects. Fixed effects represent the global relationship between explanatory and response variables, while random effects represent the deviations from the global relationships within each group that are only associated with membership to a particular group [30]. The normal global $y = f(x)$ relationship only takes the effects of explanatory variables to the regression into account, while overlooking the effects of other relevant factors (e.g., site, growth stage and cultivar type). The mixed-effect model also addresses the hierarchical nature of the data by incorporating plot or stand-level variations in the model [31,32]. Due to these advantages, the mixed-effect model has been extensively adopted in the field of forest remote sensing during recent years, with a particular focus on forest biomass estimation with LiDAR data [31–33]. Poudel et al. [32] combined linear mixed-effect (LME) models with multi-temporal LiDAR data to estimate changes of aboveground biomass and cubic volume. The authors grouped 78 plots into five plot types based on basal area per hectare in the given plots and the plot type was used as random effect. The estimation based on LME models was more accurate than that based on the differences in LiDAR-based estimates.

This study was conducted to explore the potential of mixed-effect models for estimating rice growth parameters based on the superiority of mixed-effect models to address uncertainty. Thus, the objectives of this study were to, (1) evaluate the potential of the fixed-wing UAV for crop monitoring; (2) estimate rice AGB and LAI by combining a LME model with spectral information derived from UAV multispectral images; (3) compare the performance of different retrieval methods (simple regression (SR), ANN, RF, LME) to estimate rice AGB and LAI. The result is promising to provide technical support for the monitoring of the crop growth status over large-scale farmland based on the UAV remote sensing platform.

2. Materials and Methods

2.1. Study Area and Experimental Details

Field experiments were conducted in two consecutive years (2017–2018) at the experimental station of the Taizhou National Modern Agriculture Demonstration Area located in Taizhou City, Jiangsu Province, China (119°89′E, 33°08′N) (Figure 1). Experiments were conducted with different N rates, planting patterns and rice cultivars (Table 1). In 2017, the experiment used four N rates and three planting patterns with two rice cultivars. In 2018, the experiment used four N rates and two planting methods with two rice cultivars. The distribution of total N at different growth stages was 30% before the transplanting stage, 20% at the tillering stage, 30% at the jointing stage and 20% at the booting stage.

Thirty-five ground control points (GCPs) were built and monitored in the study area (Figure 1) to enable georeferencing of the UAV data. These were set up using circular panels with a 50 cm diameter. The center of each panel was measured using the Trimble GeoExplorer 6000 Series GeoXH (Trimble Navigation, Sunnyvale, CA, USA). The estimated accuracy of the GCPs was 2.5 cm in horizontal coordinates and 4 cm in longitudinal coordinates.

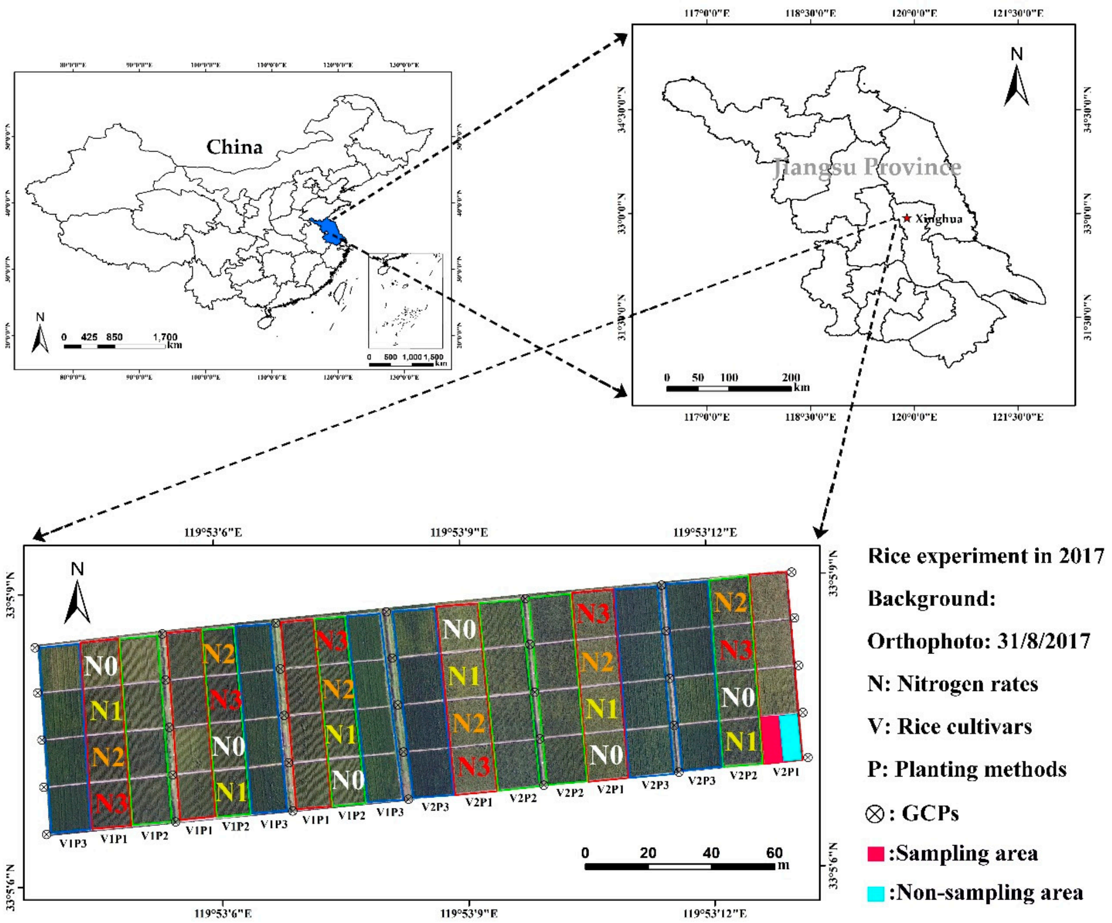

Figure 1. Study site: the rice experiment was conducted at the Taizhou Experimental Station in Jiangsu Province of China in 2017.

Table 1. Basic information about experimental design and data acquisition.

Experiment	Transplanting	Cultivars	N Rate (kg ha^{-1})	Planting Patterns	Plot Size	Sampling Stages
EXP.1 2017	14-Jun	Nanjing-9108 (Japonica) Yongyou-2640 (*Indica*/*Japonica* Hybrid)	N0(0) N1(135) N2(270) N3(405)	PMT CMT DS	150 m^2 (15 m × 10 m)	Stem elongation (25-Jul) Booting (10-Aug) Heading (23-Aug) Flowering (1-Sep) Grain filling (14-Sep)
EXP.2 2018	18-Jun	Nanjing-9108 (Japonica) Yongyou-2640 (*Indica*/*Japonica* Hybrid)	N0(0) N1(135) N2(270) N3(405)	PMT CMT	300 m^2 (20 m × 15 m)	Tillering (22-Jul) Stem elongation (28-Jul) Panicle initiation (12-Aug) Booting (19-Aug) Heading (31-Aug) Grain filling (21-Sep)

Note: PMT represents pot-seeding mechanical transplanting, CMT represents carpet-seeding mechanical transplanting and DS represents direct-sowing.

2.2. Field Data Collection

Ground destructive sampling was conducted just after the UAV campaigns at key rice growth stages (Table 1). For each plot, three hills were randomly selected from different positions in the sampling area (Figure 1) of the plot, the tiller number of which equaled the average tiller number of the plot at the corresponding growth stage. The average tiller number was determined by averaging the tiller number of 20 random hills in the sampling area at corresponding growth stages [34]. Plants were manually uprooted and separated into different organs (leaf, stem and panicle) to determine the dry matter content of different organs.

LAI were immediately measured by using a Li-3000c leaf area meter (Li-Cor., Lincoln, NE, USA) to scan the area of separated fresh green leaves. Based on Equation (1), the LAI of the rice population was calculated to represent the LAI of each plot [35].

$$\mathrm{LAI} = \frac{\mathrm{A} \times 10^{-4}}{3 \times \frac{1}{\mathrm{D}}} \tag{1}$$

D represents the number of hills in a 1-m^2 scope within the plot from a survey of the rice stem tiller dynamic at the nutritive growth stage; A (cm^2) represents the total leaf area of the sample (three hills). Descriptive statistics of growth parameters are show in Table 2.

Table 2. Descriptive statistics of growth parameters for experiments in 2017 and 2018.

Type	Variable	N	Mean	Minimum	Maximum	SD	CV (%)
Growth parameters	AGB (t ha^{-1})	648	9.05	0.54	22.83	5.22	58
	LAI	648	4.81	0.40	14.83	2.49	52

Note: N represents the number of samples, SD represents the standard deviation and CV represents the coefficient of variation.

2.3. UAV Image Acquisition

Aerial images were collected using a commercially available fixed-wing eBee SQ UAV (senseFly, Cheseaux-Lausanne, Switzerland) equipped with a compact multispectral Parrot Sequoia sensor (MicaSense, Seattle, WA, USA) (Figure 2). The eBee SQ is a hand-launched, autonomous, flying aircraft that consists of a rigid wing and an electric motor-driven pusher propeller. The maximum flight duration of the eBee SQ (equipped with multispectral sensor) is approximately 55 min during which it can cover a maximum area of about 80 ha (spatial resolution of 8 cm, both forward and lateral image overlaps of 70%). SenseFly's eMotion software was used to develop the eBee SQ flight plan beforehand and to monitor the flight using a laptop; for more detailed information, please refer to the method described by Chianucci et al. [36]. The Parrot Sequoia sensor consists of five channels, which include a 16 megapixel rolling shutter RGB camera with a 4608 × 3456 pixel resolution and four 1.5 megapixel global-shutter single band cameras at 1280 × 960 pixel resolution in the following spectral bands: green (wavelength = 550 nm, bandwidth = 40 nm), red (wavelength = 660 nm, bandwidth = 40 nm), red edge (wavelength = 735 nm, bandwidth = 10 nm) and near infrared (NIR, wavelength = 790 nm, bandwidth = 40 nm). Radiometric calibration images of the Parrot Sequoia camera were captured on the ground before each flight, using a calibrated reflectance panel (MicaSense) [37]. The Parrot Sequoia camera also depends on a sunshine sensor to automatically adjust the readings to ambient light to minimize error during image capture [38]. Absolute positioning was directly recorded with a georeferencing method using the position/attitude measurements derived from the UAV-embedded GPS/IMU instruments [36].

Flights were conducted at five sampling stages for 2017 and six sampling stages for 2018 during the growing seasons (Table 1). Images were collected in TIFF format with the camera set to automatic mode under stable ambient and clear-sky conditions between 10:00 am and 2:00 pm. The ground pixel resolution was set to 8 cm, corresponding to a flight altitude of about 80 m. The forward and lateral image overlaps were both set to 70%.

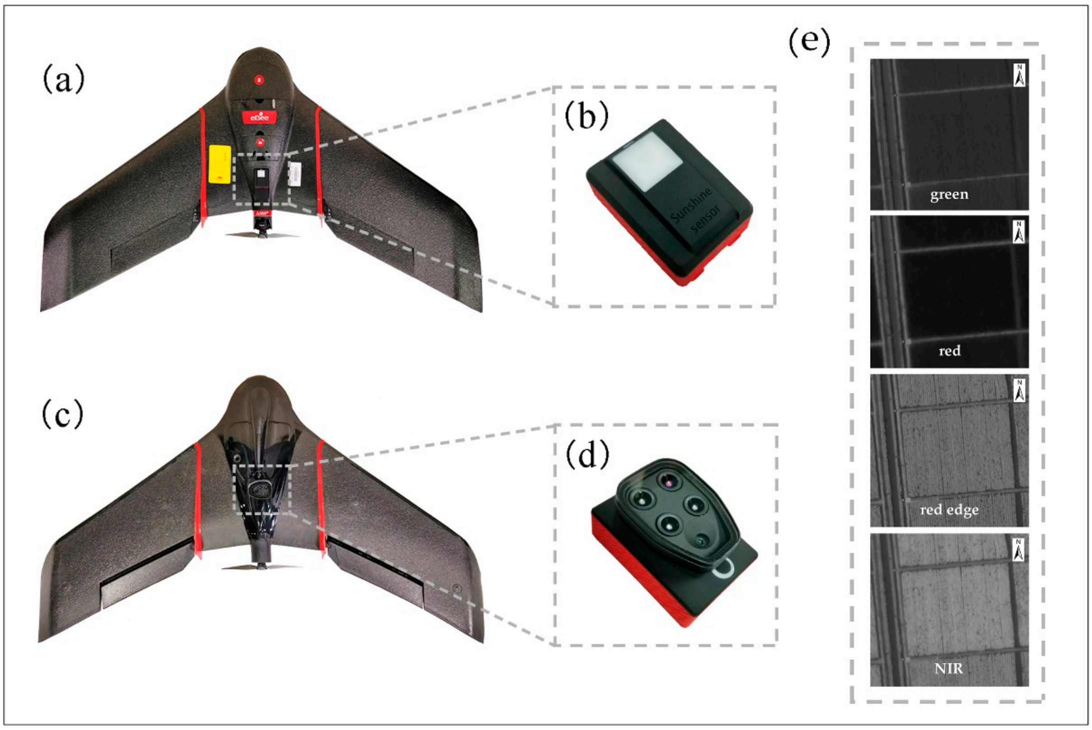

Figure 2. Unmanned aerial vehicle (UAV) platform (eBee SQ) and sensors used in this study: (**a**) Front of the UAV; (**b**) sunshine sensor; (**c**) back of the UAV; (**d**) multispectral camera; (**e**) truncated images of four magnified orthomosaic images generated at the stem elongation stage.

2.4. Processing of UAV Spectral Images

After each flight, five image sets were produced: one multispectral image sets each in the green, red, red edge and NIR bands and one RGB image set. Only the four multispectral image sets were selected because VIs and four monochrome image reflectance were needed for this study. Pix4D mapper 4.2 (Pix4D S.A., Lausanne, Switzerland) was used to generate the orthomosaic. The key steps of orthomosaic generation using Pix4D mapper comprised camera alignment, geo-referencing, radiometric calibration, orthomosaic and generating VI maps. 35 GCPs in the Pix4D project were used to georeference the study area, increase the global accuracy and decrease band-to-band misalignment. Reflectance calibration was conducted by using radiometric calibration images with known reflectance values provided by MicaSense. Eight VI maps were produced by using the index calculator of the Pix4D mapper. These VIs are listed in Table 3 and are commonly used for AGB and LAI estimation [39–47].

Table 3. Selected vegetation indices used for aboveground biomass and leaf area index estimation.

Vegetation Index	Formulation	Application	Reference
NDVI	$(R_{790} - R_{660})/(R_{790} + R_{660})$	AGB & LAI	[39]
NDRE	$(R_{790} - R_{735})/(R_{790} + R_{735})$	AGB & LAI	[40]
CI_{RE}	$(R_{790}/R_{735}) - 1$	AGB & LAI	[41]
MSAVI	$0.5\left[2R_{790} + 1 - \sqrt{(2R_{790}+1)^2 - 8(R_{790} - R_{660})}\right]$	AGB & LAI	[42]
OSAVI	$(1 + 0.16)(R_{790} - R_{660})/(R_{790} + R_{660} + 0.16)$	AGB & LAI	[43]
MCARI1	$1.2[2.5(R_{790} - R_{660}) - 1.3(R_{790} - R_{560})]$	AGB & LAI	[44]
MTVI2	$1.5(1.2(R_{790} - R_{550}) - 2.5(R_{660} - R_{550}))/\sqrt{(2R_{790}+1)^2 - \left(6R_{790} - 5\sqrt{R_{660}}\right) - 0.5}$	AGB	[45]
DATT	$(R_{790} - R_{735})/(R_{790} - R_{660})$	AGB	[46]
GNDVI	$(R_{790} - R_{560})/(R_{790} + R_{560})$	LAI	[47]
MTVI1	$1.2[1.2(R_{790} - R_{560}) - 2.5(R_{660} - R_{560})]$	LAI	[45]

With ENVI 5.3 (Exelis Visual Information Solutions, Boulder, CO, USA), the non-sampling area (Figure 1) of each plot in one orthomosaic image was manually outlined as a “Region of Interest” to extract the average VI. The descriptive statistics of all VIs are show in Table 4.

Table 4. Descriptive statistics of vegetation indices for the experiments in 2017 and 2018.

Type	Variable	N	Mean	Minimum	Maximum	SD	CV (%)
Vegetation indices	NDVI	648	0.87	0.51	0.94	0.07	8
	NDRE	648	0.33	0.05	0.47	0.09	28
	CI_{RE}	648	1.02	0.11	1.76	0.38	37
	MSAVI	648	0.65	0.16	0.91	0.18	27
	OSAVI	648	0.73	0.31	0.90	0.11	16
	MCARI1	648	0.31	0.01	0.91	0.17	55
	MTVI1	648	0.61	0.15	1.13	0.18	29
	MTVI2	648	0.69	0.16	0.97	0.19	28
	DATT	648	0.52	0.12	0.66	0.11	22
	GNDVI	648	0.74	0.39	0.85	0.08	11

Note: N represents the number of samples, SD represents the standard deviation and CV represents the coefficient of variation.

2.5. AGB and LAI Retrieval Methods

To improve the applicability of the regression model, the data obtained from the two years of experiments were used to examine the relationships between remote sensing variables and AGB or LAI. Four models (SR, ANN, RF and LME) were used to quantify the relationship between remote sensing variables and AGB or LAI. Of these methods, SR is a parametric regression model and the others are non-parametric regression models. All analyses were respectively performed within three growth stage groups, that is, the whole season, pre-heading stages (stages before heading) and post-heading stages (stages after heading).

2.5.1. Baseline Retrieval Methods

In this study, three baseline retrieval methods for crop monitoring (SR, ANN and RF) were used for AGB and LAI retrieval. The statistical analyses for SR and ANN were performed using SPSS 25.0 software (SPSS, IBM, IL, USA) while RF was executed in R.3.2.0 (R Foundation for Statistical Computing, Vienna, Austria). Plots were created in GraphPad Prism 6.0 (GraphPad Software, San Diego, CA, USA).

SR models include both linear and nonlinear (exponential) regression models. The basic function forms of linear (Equation (2)) and exponential (Equation (3)) regressions are given by:

$$y = a_0 + a_1 x \tag{2}$$

$$y = b_0 e^{b_1 x} \tag{3}$$

where the independent variable x represents the explanatory variable (VI), the dependent variable y represents the response variables (AGB and LAI) and parameters a_0, a_1, b_0 and b_1 are estimated by minimizing the least square error. The performance of various regression models is assessed by comparing their coefficient of determination (R^2) (Equation (8)) and root mean square error (RMSE) (Equation (9)).

The ANN regression model is based on a gradient learning method, which can realize strong nonlinear mapping between input and output [19]. ANN contains a large number of processing elements (neurons), which are arranged in different layers in a network: an input layer, an output layer and one or more hidden layers [18]. In this study, the number of hidden layers was set to 1. The number of neurons was modified by repeating the setting. Via cross-validation, the coefficient of determination (R^2) (Equation (8)) and root mean square error (RMSE) (Equation (9)) from test samples were compared. After comparing the values of R^2 and RMSE, the most appropriate numbers were obtained. The scaled conjugate gradient was also selected as training algorithm. Figure 3 shows a schematic of the initial neural network model.

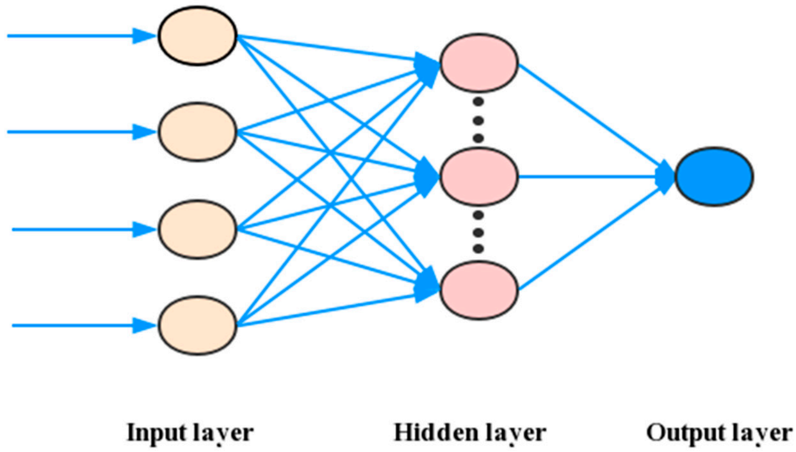

Figure 3. Schematic of the initial neural network model.

The RF model is derived from the classification tree algorithm and can be used for both classification or regression [48]. An RF model has two parameters: the number of decision trees (Ntree) and the minimum number of observations per tree leaf (mtry). In this research, the RF regression model used relevant parameters that were reported in prior studies, Ntree was set to 500 and mtry was set to 2 for the whole season and different stage groups [19,24].

2.5.2. Linear Mixed-effect Model

The LME model was also used for AGB and LAI retrieval. The LME model was executed using SPSS 25.0 software (SPSS) while plots were created using Graph-Pad Prism (GraphPad Software, San Diego, CA, USA). The LME incorporates two parameters: fixed and random effects [49]. The fixed effects are parameters that are associated with an entire population or with certain repeatable levels of experimental factors; the random effects are parameters associated with individual experimental units drawn at random from the population [30]. The form of the LME model is given by:

$$y = \mathrm{X}\beta + \mathrm{Z}u + \varepsilon \tag{4}$$

where y represents a $N \times 1$ column vector, the response variable; X represents a $N \times p$ design matrix of the p predictor variables; β represents a $p \times 1$ column vector of the fixed-effects regression coefficients; Z represents the $N \times q$ design matrix for q random effects (the random complement to the fixed X); u represents a $q \times 1$ vector of the random effects (the random complement to the fixed β); and ε represents a $N \times 1$ column vector of the residuals, part of which is not explained by the model, Xβ + Zu.

$$u \sim N(0, \mathrm{G}), \varepsilon \sim N(0, \mathrm{R}) \tag{5}$$

$$\mathrm{G} = \sigma_s^2 H(\phi) \tag{6}$$

$$\mathrm{R} = \tau^2 \cdot I \tag{7}$$

where G represents the variance-covariance matrix of the random effects. $H(\cdot)$ is defined by the suitable correlation function $f(h, \phi)$, σ_s^2 represents the *partial sill*, ϕ represents the *range* and h represents the *lag* or distance [50]. R represents a $N \times N$ positive definite variance-covariance matrix of ε. τ^2 is called the *nugget effect*. I represents the identity matrix (diagonal matrix of 1s). ε is not correlated with the random effect u, that is, $Cov(u, \varepsilon) = 0$.

Simultaneous estimates of correlation parameters (i.e., σ_s, h, ϕ and τ) and fixed effect coefficients (i.e., β) were obtained by restricted (or residual) maximum likelihood estimation (REML) [50], to reflect the loss of degrees of freedom due to the estimation of the fixed effects coefficients [51]. For both AGB and LAI models, the reflectance of four spectral bands (green, red, red-edge and NIR) were set as fixed effects for the whole season and different stage groups. Random effects have different choices, including three individual factors: cultivar (C, which is a factor variable with two types), planting pattern (P, which is a factor variable with three types), growth stage (S, which is a factor variable with seven types) and their combinations (CP, CS, PS and CSP). The rice population structure is an important indicator for rice growth and rice with the same population structure is relatively homogeneous. These three individual factors (C, S and P) contribute strongly to the formation of rice population and were selected as candidates of random effects [52,53]. Moreover, with these random effects, more group combinations and dataset with greater variability were utilized to improve the robustness of the LAI/AGB models in this study.

With different random effects, Z and u have different dimensions. For instance, if cultivar and growth stage (CS) are set as random effects, the data will be broken down into $2 \times 7 = 14$ groups, where Z will be a $N \times 14$ design matrix and u will be a 14×1 vector of the random effects. Optimal random effects were determined by comparing the RMSE values.

2.6. Comparison of Different Models

Comparisons of different models were achieved by evaluating their predictive capabilities, which were evaluated by their coefficient of determination (R^2) (Equation (8)) and RMSE (Equation (9)) using a k-fold (k = 10) cross-validation procedure.

$$R^2 = \frac{\sum_{i=1}^{n}(x_i - \overline{x})^2 (y_i - \overline{y})^2}{\sum_{i=1}^{n}(x_i - \overline{x})^2 \sum_{i=1}^{n}(y_i - \overline{y})^2} \tag{8}$$

$$\mathrm{RMSE} = \sqrt{\frac{1}{n}\sum_{i=1}^{n}(x_i - y_i)^2} \tag{9}$$

where x_i and y_i represent the estimated and measured values (AGB or LAI), $\overline{x}$ and $\overline{y}$ represent the average estimated and measured values and n represents the sample number.

3. Results

3.1. Relationships between AGB and LAI with VIs Extracted from Multispectral Images

AGB and LAI are the major growth indicators for the monitoring of the rice growth status. Figure 4 shows the relationships between rice AGB and VIs that are generally used for biomass estimation; the best-fit form of the curve is an exponential regression. For the whole season, NDRE and DATT both performed best amongst all VIs and explained 68% of the variability in AGB (Figure 4b,g). For pre-heading stages, NDRE, CI_{RE} and DATT achieved better performance ($R^2 > 0.70$, RMSE < 2.29 t ha^{-1}, Figure 4b,c,g) than other VIs (R^2: 0.51–0.57, RMSE: 3.12–3.39 t ha^{-1}). However, for post-heading stages, all selected VIs were weakly related to AGB with the highest R^2 values of 0.25 and the lowest RMSE values of 3.49 t ha^{-1} (DATT).

Figure 5 shows the relationships between LAI and VIs that are commonly used for LAI estimation. The best curve form is also the exponential regression. For the whole season, NDRE, GNDVI and CI_{RE} outperformed other VIs, with R^2 values ranging from 0.72–0.74 and RMSE values ranging from 1.46–1.59 (Figure 5b,c,d). For pre-heading stages, NDRE performed best and explained 76% variability in LAI (Figure 5b). Other VIs achieved good performance with R^2 values ranging from 0.66–0.74 and RMSE values ranging from 1.33–1.70 except for MTVI1 (Figure 5h). For post-heading stages, all selected VIs had weaker relationships with LAI compared to other stage groups, with highest R^2 values of 0.56 and lowest RMSE values of 1.60.

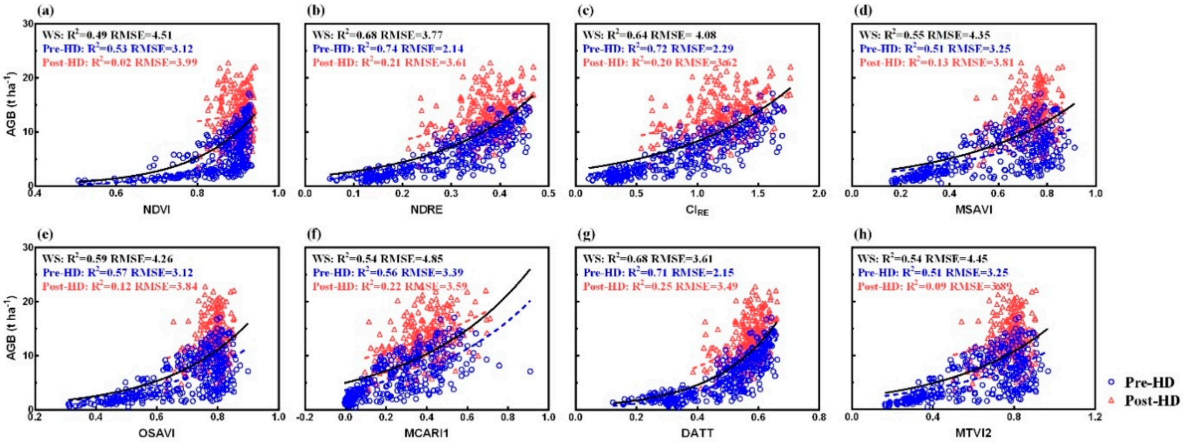

Figure 4. Aboveground biomass (t ha^{-1}) plotted against vegetation indices: (**a**) NDVI; (**b**) NDRE; (**c**) CI_{RE}; (**d**) MSAVI; (**e**) OSAVI; (**f**) MCARI1; (**g**) DATT; (**h**) MTVI2. WS represents the whole season, Pre-HD represents pre-heading stages and Post-HD represents post-heading stages.

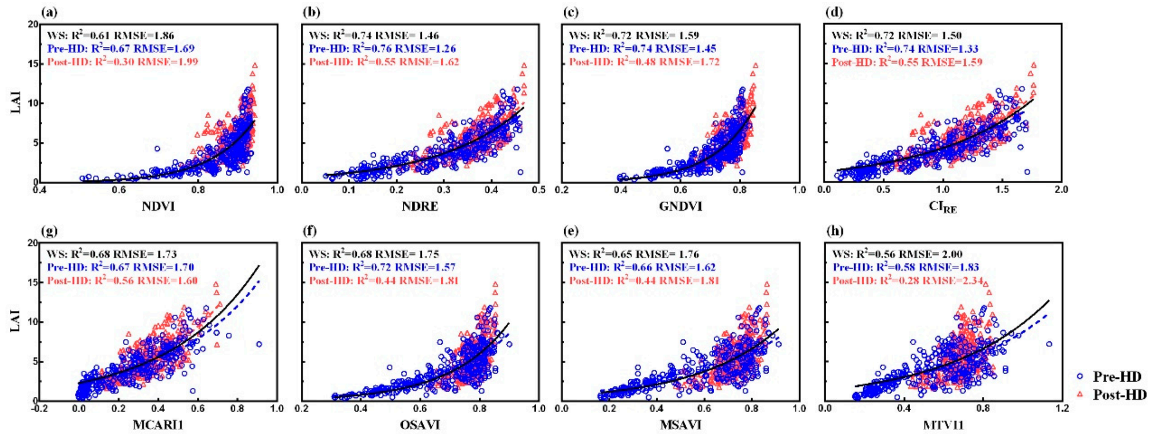

Figure 5. Leaf area index plotted against vegetation indices: (**a**) NDVI; (**b**) NDRE; (**c**) GNDVI; (**d**) CI_{RE}; (**e**) MCARI1; (**f**) OSAVI; (**g**) MSAVI; (**h**) MTVI1. WS represents the whole season, Pre-HD represents pre-heading stages and Post-HD represents post-heading stages.

VIs extracted from multispectral images explained the variability of AGB and LAI for the whole season and pre-heading stages, while the relationships between AGB and LAI with the VIs were relatively poor for post-heading stages.

3.2. Determination of Model Parameters for ANN, RF and LME Models

It is critical to identify appropriate model parameters with which to develop the monitoring model. In the ANN model, numbers from 3 to 30 neurons were attempted and the optimal parameter was obtained when R^2 reached a maximum and the RMSE reached a minimum on test dataset via cross validation. The parameters for the final models (ANN and RF) are shown in Table 5.

Different random effect combinations and their RMSE values are shown in Figure 6. Optimal random effects were determined by comparing RMSE value results. For the LME model of AGB (Figure 6a), the CSP (i.e., the combination of cultivar, planting method and growth stage) resulted in the minimum RMSE for the whole season and for different stage groups. For the LME model of LAI (Figure 6b), the CSP combination resulted in minimum RMSE values for the whole season and different stage groups. As a result, the combination of cultivar, planting method and growth stage was set as random effects for both AGB and LAI models.

Table 5. Parameters for artificial neural networks (ANN) and random forests (RF) regression models.

Growth Index	Growth Stage	ANN Model Parameter	
		Number of Hidden Neurons	Training Algorithm
AGB	WS	27	Scaled Conjugate Gradient
	Pre-HD	21	
	Post-HD	23	
LAI	WS	17	Scaled Conjugate Gradient
	Pre-HD	15	
	Post-HD	14	

Note: WS represents the whole season, Pre-HD represents pre-heading stages and Post-HD represents post-heading stages.

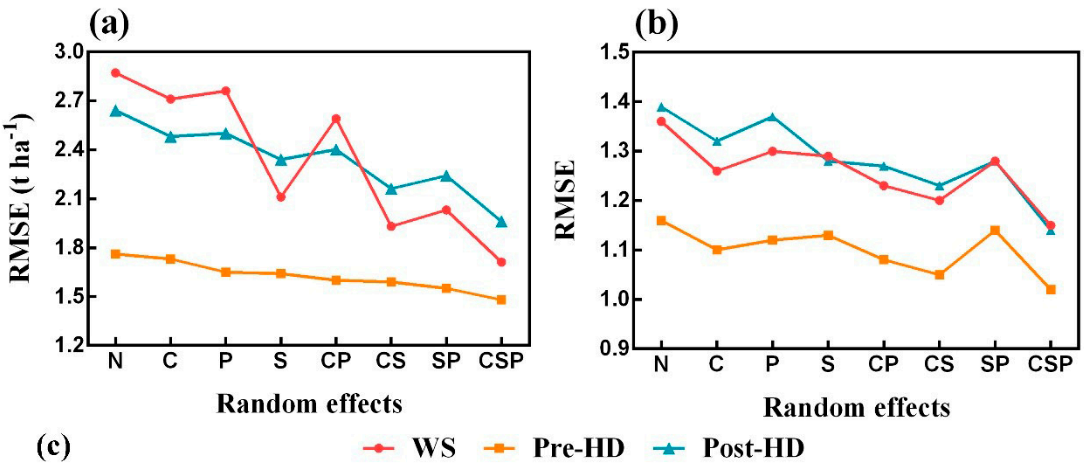

(c)

Random effects	N	C	P	S	CP	CS	SP	CSP
Number of Groups	0	2	3	7	6	14	18	36
Samples per Group	576	288	96-240	48-120	48-120	24-60	24-48	12-24

Figure 6. Determination of optimal model parameters (random effects) for linear mixed-effect (LME) model using RMSE: (**a**) AGB; (**b**) LAI; (**c**) grouping situation with different random effects. N represents no random effects (fixed effects only). C represents cultivar, P represents planting method, S represents growth stage, WS represents the whole season, Pre-HD represents pre-heading stages and Post-HD represents post-heading stages.

3.3. Comparative Analysis of Four Models Based on Predictive Capability

The LME model was applied to estimate both rice AGB and LAI and a comparative analysis between the LME model and the other three frequently-used models (including a parametric regression model (SR) and two non-parametric regression models (ANN and RF)) was conducted using k-fold (k = 10) cross-validation.

For AGB estimation, Figure 7 displays scatter diagrams of measured AGB values versus estimated values derived from SR (with the best performing VI), ANN, RF and LME models for whole season and different stage groups. For the whole season, SR produced the highest estimation accuracy using DATT, with R^2 and RMSE values of 0.54 and 3.55 t ha^{-1}, respectively (Figure 7a). ANN and RF outperformed SR with respective R^2 values of 0.75 and 0.70 and RMSE values of 2.63 t ha^{-1} and 2.86 t ha^{-1} (Figure 7d,g). The LME model significantly improved estimation accuracy (R^2 = 0.89 and RMSE = 1.75 t ha^{-1}) (Figure 7j) and was superior to other models. For the pre-heading stages, SR achieved the highest estimation accuracy (R^2 = 0.71 and RMSE = 2.10 t ha^{-1}) using DATT (Figure 7b). Compared to SR, slight improvements were obtained by ANN (R^2 = 0.79 and RMSE = 1.80 t ha^{-1}) (Figure 7e) and RF (R^2 = 0.73 and RMSE = 2.03 t ha^{-1}) (Figure 7h). Moreover, the LME model achieved moderate improvements with R^2 and RMSE values of 0.86 and 1.49 t ha^{-1}, respectively (Figure 7k). For the post-heading stages, SR had the highest estimation accuracy using DATT but remained low (R^2 = 0.22 and RMSE = 3.49 t ha^{-1}) (Figure 7c). In contrast, ANN and RF outperformed SR, with respective R^2 values of 0.54 and 0.40 and RMSE values of 2.69 t ha^{-1} and 3.06 t ha^{-1} (Figure 7f,i). The LME model significantly improved the AGB estimation accuracy (R^2 = 0.75 and RMSE = 1.97 t ha^{-1}) (Figure 7l) compared to the other tested models. Therefore, the LME model is suggested as a promising model for improving AGB estimation for all growth stages.

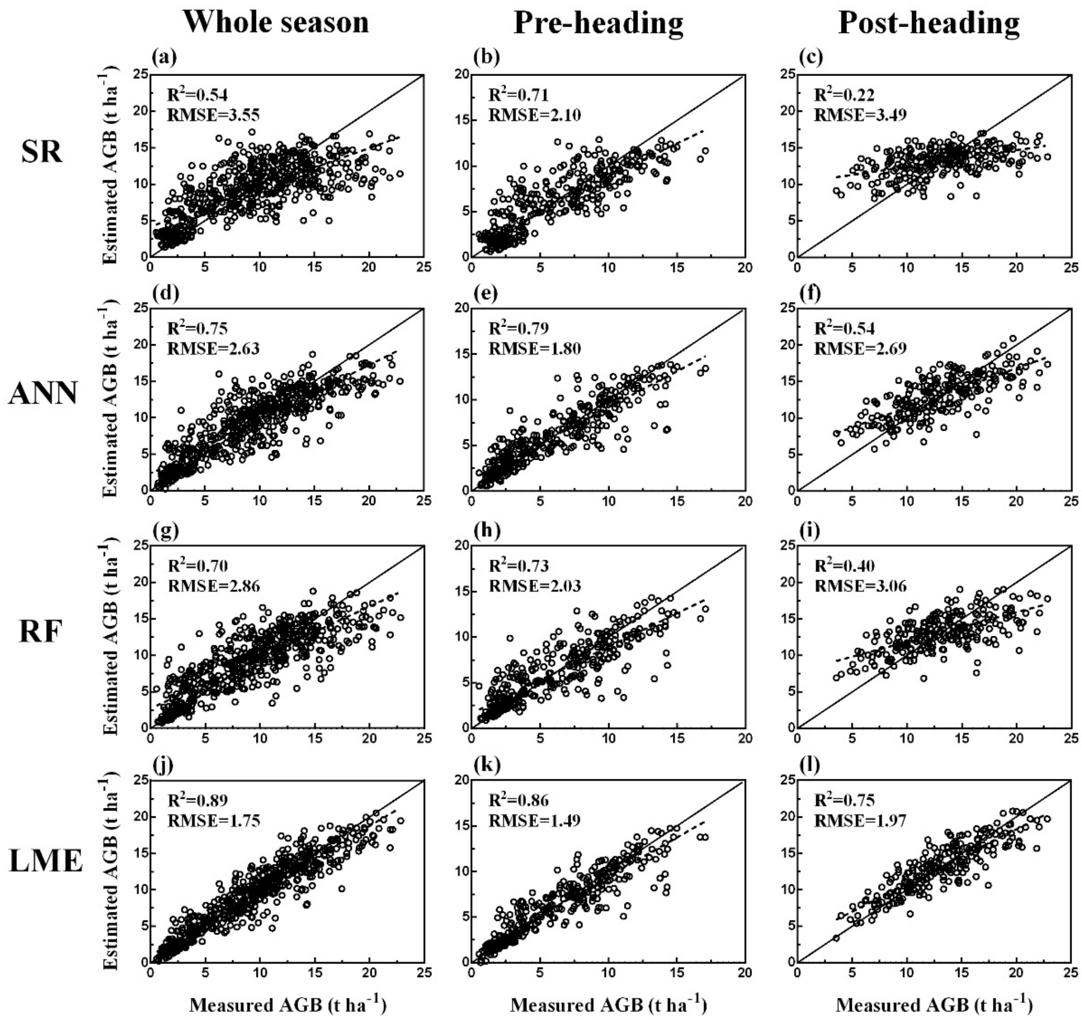

Figure 7. Validation of above ground biomass (AGB) estimation models for the whole season and different stage groups: (**a**) SR for the whole season, (**b**) pre-heading stages and (**c**) post-heading stages; (**d**) ANN for the whole season, (**e**) pre-heading stages and (**f**) post-heading stages; (**g**) RF for the whole season, (**h**) pre-heading stages and (**i**) post-heading stages; (**j**) LME model for the whole season, (**k**) pre-heading stages and (**l**) post-heading stages.

For LAI estimation, Figure 8 shows the scatter diagrams for measured LAI values versus estimated values derived from SR (with the best performing VI), ANN, RF and LME models for the whole season and for different stage groups. For the whole season, SR achieved the highest estimation accuracy using NDRE, with R^2 and RMSE values of 0.66 and 1.45, respectively (Figure 8a). In contrast, ANN and RF slightly increased estimation accuracy, with respective R^2 values of 0.74 and 1.27, RMSE values of 1.27 and 1.36 (Figure 8d,g). The LME model yielded more accurate estimation results than the other models (R^2 = 0.79 and RMSE = 1.15) (Figure 8j). For pre-heading stages, SR achieved the highest estimation accuracy (R^2 = 0.73 and RMSE = 1.25) using NDRE (Figure 8b). The accuracies of ANN and RF were approximately equal to that of SR, with respective R^2 values of 0.75 and 0.74 and RMSE values of 1.19

and 1.22 (Figure 8e,h). In contrast, the LME model outperformed the other models (R^2 = 0.81 and RMSE = 1.04) (Figure 8k). For post-heading stages, SR achieved the highest estimation accuracy using CI_{RE}, with respective R^2 and RMSE values of 0.53 and 1.59 (Figure 8c). ANN and RF slightly improved the estimation accuracy, with respective R^2 values of 0.58 and 0.56 and RMSE values of 1.49 and 1.53 (Figure 8f,i). The LME model yielded the most accurate estimation across all models (R^2 = 0.76 and RMSE = 1.16) (Figure 8l). Therefore, the LME model performed better in estimating rice LAI.

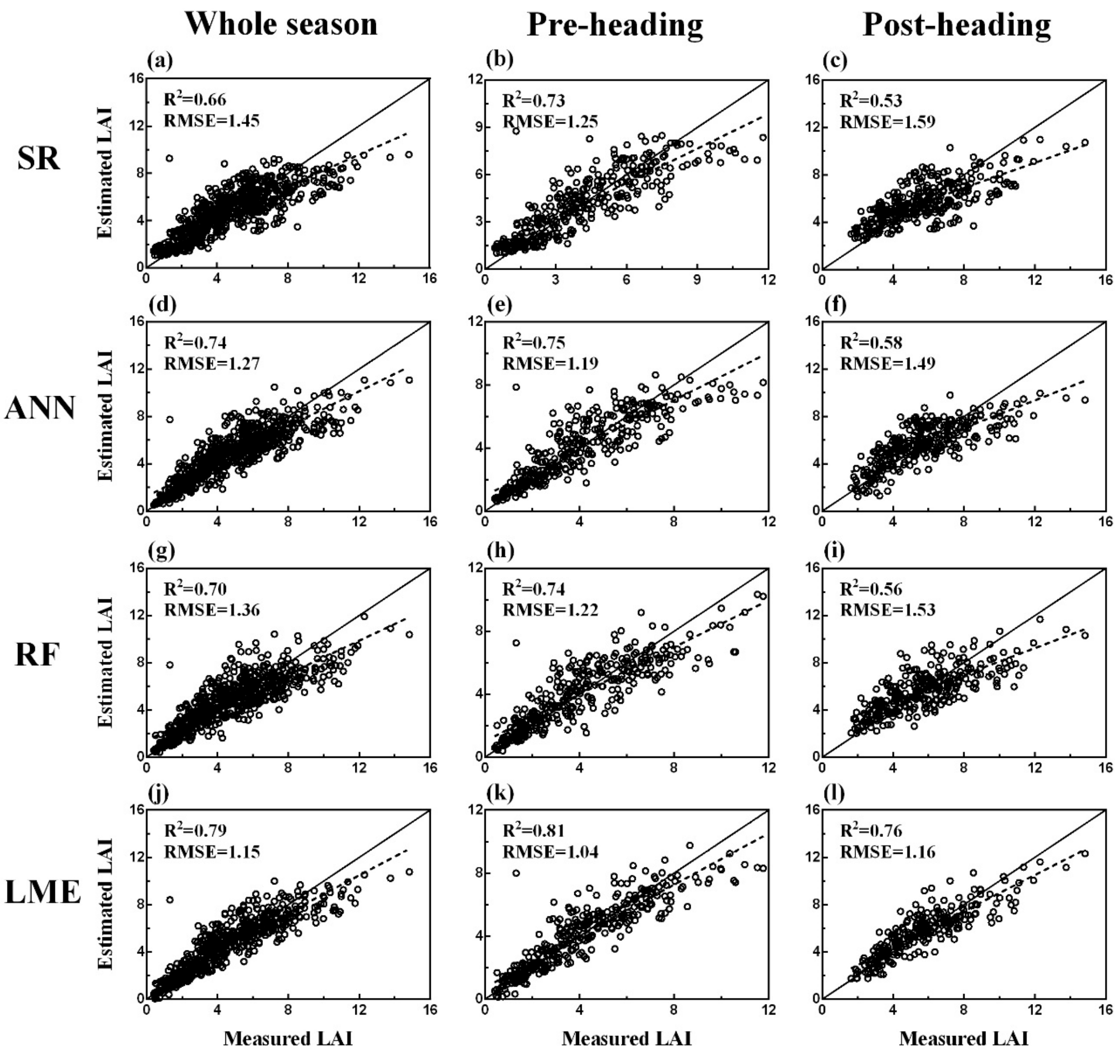

Figure 8. Validation of LAI estimation models for the whole season and different stage groups: (**a**) SR for the whole season, (**b**) pre-heading stages and (**c**) post-heading stages; (**d**) ANN for the whole season, (**e**) pre-heading stages and (**f**) post-heading stages; (**g**) RF for the whole season, (**h**) pre-heading stages and (**i**) post-heading stages; (**j**) LME model for the whole season, (**k**) pre-heading stages and (**l**) post-heading stages.

In addition, although the LME model improved the estimation accuracy of both AGB and LAI, their degree of improvement differed. For AGB estimation, compared to SR (Figure 7a–c), the R^2 of the LME model increased by 0.35 for the whole season, by 0.15 for the pre-heading stages and by 0.53 for the post-heading stages, while the corresponding RMSE values decreased by 1.8 t ha^{-1}, 0.61 t ha^{-1} and 1.52 t ha^{-1}, respectively (Figure 7j–l). For LAI estimation, compared to SR (Figure 8a–c), the LME model R^2 increased by 0.13 for the whole season, by 0.08 for the pre-heading stages and by 0.23 for the post-heading stages; corresponding RMSE values decreased by 0.30, 0.21 and 0.43, respectively (Figure 8j–l). Consequently, the LME model may be more suitable for rice AGB estimation.

3.4. Comparison of LME Models with Different Random Effects

It is necessary to analyze the results for all combinations of random effects to evaluate the predictive capability within the groups of LME models. Practical application should be expanded on; the results show that the method can be used to make predictions within a single known group as well as across multiple different groups. Groupings do not have to be CSP and it is not the optimal choice for the random effects. Furthermore, similar results were obtained from the LME model of AGB (Figures 9 and 10) and that of LAI (Figures 11 and 12). The analysis was conducted based on the LME model of the AGB.

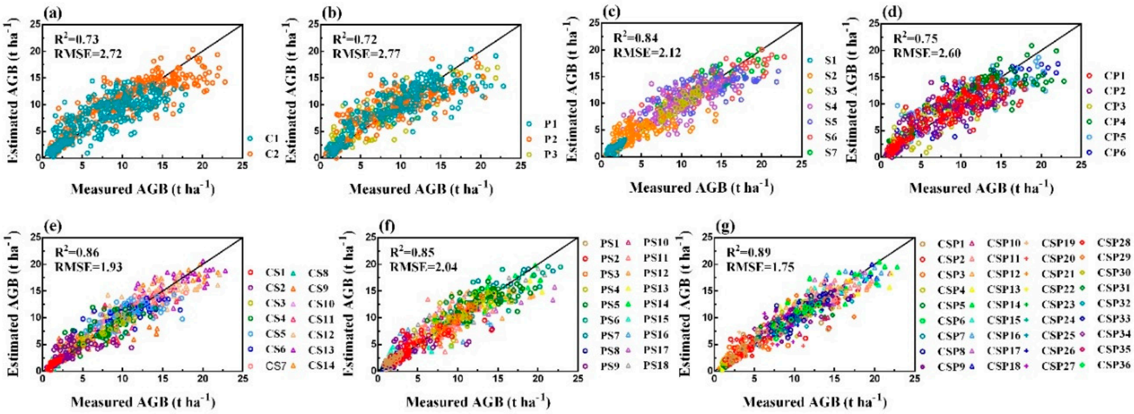

Figure 9. Comparison of LME models (for AGB estimation) with different random effects: (**a**) C, cultivar, (**b**) P, planting pattern, (**c**) S, growth stage, (**d**) CP, combination of cultivar and planting pattern, (**e**) CS, combination of cultivar and growth stage, (**f**) PS, combination of planting pattern and growth stage and (**g**) CSP, combination of cultivar, growth stage and planting pattern. C1-2, P1-3, S1-7, CP1-6, CS1-14, PS1-18 and CSP1-36 represent the groupings of corresponding random effects, respectively.

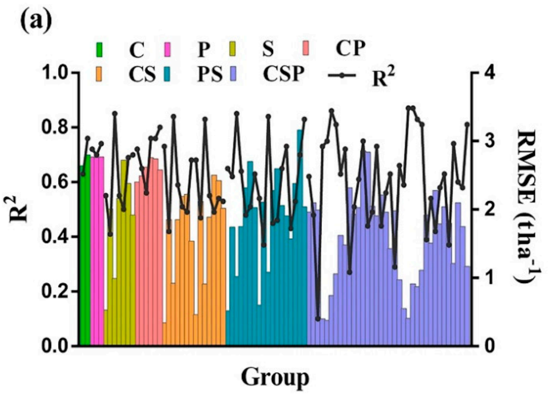

(b)

Groups	Average R^2	Average RMSE (t ha^{-1})
C1-2	0.70	2.72
P1-3	0.72	2.77
S1-7	0.61	1.82
CP1-6	0.71	2.60
CS1-14	0.60	1.66
PS1-18	0.61	1.88
CSP1-36	0.60	1.60

Figure 10. Comparison of predictive capability within the groups of LME models (for AGB estimation) using different random effects: (**a**) the R^2 and RMSE of the groups of different random effects; (**b**) the average R^2 and RMSE of the groupings of different random effects. C represents cultivar; P represents planting pattern; S represents growth stage; CP represents combination of cultivar and planting pattern; CS represents combination of cultivar and growth stage; PS represents combination of planting pattern and growth stage; CSP represents combination of cultivar, growth stage and planting pattern.

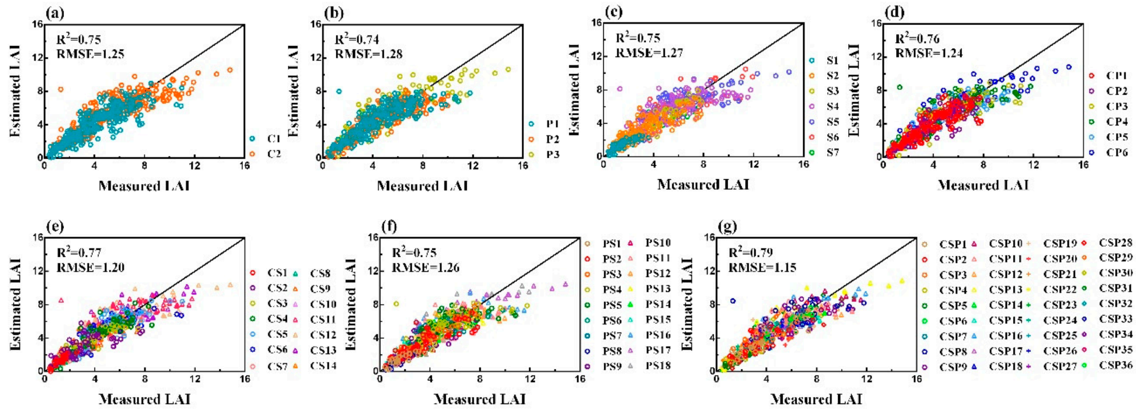

Figure 11. Comparison of LME models (for LAI estimation) with different random effects: (**a**) C, cultivar, (**b**) P, planting pattern, (**c**) S, growth stage, (**d**) CP, combination of cultivar and planting pattern, (**e**) CS, combination of cultivar and growth stage, (**f**) PS, combination of planting pattern and growth stage and (**g**) CSP, combination of cultivar, growth stage and planting pattern. C1-2, P1-3, S1-7, CP1-6, CS1-14, PS1-18 and CSP1-36 represent the groupings of corresponding random effects, respectively.

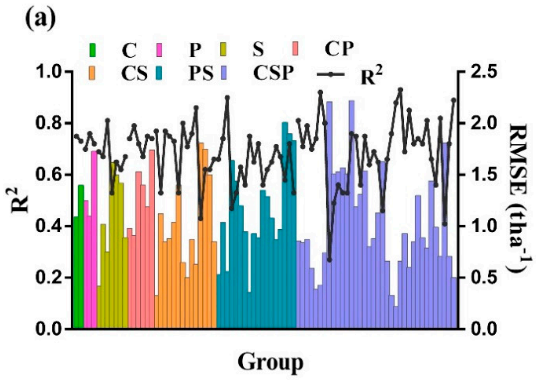

(b)

Groups	Average R^2	Average RMSE
C1-2	0.74	1.25
P1-3	0.73	1.36
S1-7	0.66	1.09
CP1-6	0.74	1.29
CS1-14	0.68	1.01
PS1-18	0.65	1.16
CSP1-36	0.69	1.03

Figure 12. Comparison of predictive capability within the groups of LME models (for LAI estimation) using different random effects: (**a**) the R^2 and RMSE of the groups of different random effects; (**b**) the average R^2 and RMSE of the groupings of different random effects. C represents cultivar; P represents planting pattern; S represents growth stage; CP represents combination of cultivar and planting pattern; CS represents combination of cultivar and growth stage; PS represents combination of planting pattern and growth stage; CSP represents combination of cultivar, growth stage and planting pattern.

Figure 9 shows the scatter diagrams for measured AGB values versus estimated values derived from LME models, which were built with different random effects. From the overall performance of modelling, CSP (the combination of cultivar, growth stage and planting pattern) performed best (R^2 = 0.89, RMSE = 1.75 t ha^{-1}) (Figure 9g). Models that included random effects of growth stage (S) obtained higher prediction accuracy (R^2: 0.84–0.89, RMSE: 1.75–2.12 t ha^{-1}) (Figure 9c,e,f,g) than other models. In particular, the LME model only used growth stage as random effect and obtained satisfactory estimation accuracy (R^2 = 0.84, RMSE = 2.12 t ha^{-1}) (Figure 9c). Therefore, growth stage could be an important factor for the rice LME model.

In addition, Figure 9 shows the modelling performance within the groups of LME models. The results indicate that models, which were segmented into more groups (number of groups ≥ 7) obtained higher prediction accuracy (R^2: 0.84–0.89, RMSE: 1.75–2.12 t ha^{-1}) (Figure 9c,e,f,g). In contrast, models with fewer groups (number of groups < 7) performed worse (R^2: 0.72–0.75, RMSE: 2.60–2.77 t ha^{-1}) (Figure 9a,b,d). This indicates that segmentation of the data inherently improved the results because it learned the mean of the segment; consequently, adding the number of groups could increase prediction accuracy. As shown in Figures 9 and 10, the LME models using C, P or CP as random effects achieved a similar performance within groups to overall model performance

(C: R^2 = 0.73, RMSE = 2.72 t ha^{-1}; P: R^2 = 0.72, RMSE = 2.77 t ha^{-1}; CP: R^2 = 0.75, RMSE = 2.60 t ha^{-1}), with average R^2 of 0.70, 0.72 and 0.71 and average RMSE of 2.72 t ha^{-1}, 2.77 t ha^{-1} and 2.60 t ha^{-1}, respectively (Figure 9a,b,d, Figure 10a,b). These models have fewer groups and the highest number of groups is only six (CP). For LME models with more segments (i.e., the models using S, CS and PS as random effects), the model performance within groups was poorer than the overall model performance (S: R^2 = 0.84, RMSE = 2.12 t ha^{-1}; CS: R^2 = 0.86, RMSE = 1.93 t ha^{-1}; PS: R^2 = 0.85, RMSE = 2.04 t ha^{-1}), with average R^2 of 0.61, 0.60 and 0.61 and average RMSE of 1.82 t ha^{-1}, 1.66 t ha^{-1} and 1.88 t ha^{-1}, respectively (Figure 9c,e,f, Figure 10a,b). Still, these models successfully yielded predictions within the groups, since almost all R^2 values of groups ranged from 0.4–0.9 (average R^2 > 0.60) (Figure 10a,b). This indicated that the LME model offered advantages beyond simply learning the mean of the segment. With regard to the LME model using CSP, the R^2 and RMSE within the groups fluctuated greatly, with R^2: 0.1–0.87, RMSE: 0.38–2.86 t ha^{-1} (Figure 10a). The result could be ascribed to the fact that the data were segmented into too many groups (number of groups = 36) when using CSP as random effects. Therefore, the number of points per group was very low (i.e., 12–24) and the modelling performance within the groups suffered from randomness and strong uncertainty. Even though the LME model (using CSP) achieved good performance over all data, this approach would lose statistical significance and simply yield the mean for the group. Consequently, for the practical application of the LME model, the CSP may be not suitable as the random effects given model generalizability. LME models with fewer segments might be promising alternatives, such as the models using S, CS or PS.

4. Discussion

4.1. Advantages of Fixed-Wing UAVs

A low-altitude UAV platform is an affordable and precise tool for the mapping of crop traits and can meet the central requirements of spatial, spectral and temporal resolutions [10]. Among various UAVs, the multi-rotor UAV has been increasingly employed in recent years due to its high stability, superior image quality and good controllability (easy take-off and landing) [17]. Nevertheless, high stability can be a double-edged sword: it provides high quality images but it also limits the multi-rotor UAV flight speed and duration [17]. As an illustration, a multi-rotor UAV required approximately 10 min to cover 1 ha (30–50 m flight altitude) for dynamic wheat NDVI monitoring [9]. Zhang et al. [54] monitored field crop conditions with a multi-rotor UAV (Aeryon Labs Inc., Waterloo, Canada), which has a maximum flight duration of 25 min and can cover close to 10 ha (120 m flight altitude) per battery charge. Compared to a multi-rotor UAV for crop monitoring, fixed-wing UAVs are competitive because they are more efficient and can cover larger areas [17]. For example, a fixed-wing UAV covered an area of 148 ha within 45 min and achieved a total flight duration of up to 60 min [55]. The fixed-wing UAV used in this study was able to cover about 80 ha with a maximum duration of 55 min (80 m flight altitude). A comparison of the flight efficiency for both types of UAVs is shown in Table 6.

Table 6. Flight efficiency comparison for two types of UAVs.

Type	No.	Maximum Speed (m s^{-1})	Endurance (min)	Reference
Multi-rotor	MR I	Not given	16–22	[9]
(MR)	MR II	13	25	[54]
	MR III	12	15	[10]
Fixed-wing	FW I	17.5	60	[55]
(FW)	FW II	33	120–360	[56]
	FW III	30	55	This paper

This study used an advanced fixed-wing UAV with a compact multispectral sensor Parrot Sequoia to monitor the crop growth status. The fixed-wing has a good flight control system and creates a relatively stable flight attitude. It can also withstand strong wind speeds of up to 12 m s^{-1}. With regard to the SR (most commonly used) validation results, a moderate result (R^2 = 0.54 and

RMSE = 3.55 t ha^{-1} from DATT) was obtained for AGB for the whole season and a better result was obtained for LAI for the whole season, with respective R^2 and RMSE values of 0.66 and 1.45. Compared to the estimation models based on multi-rotor UAVs (e.g., the best AGB results acquired by best performing VI (R^2 = 0.55, RMSE = 2.77 t ha^{-1}) by Zheng et al. [57] and the best LAI model produced by a three-band vegetation index modified triangular vegetation index (MTVI2) with respective R^2 and relative root mean squared error (RRMSE) values of 0.80 and 24% reported by Yao et al. [11]), the results obtained with the fixed-wing UAV in this study were relatively reliable.

4.2. Relationship between Growth Parameters and Vegetation Indices

SR has been widely used to explore the relationship between crop growth parameters and VIs, which resulted in the development of a large number of multispectral VIs [11,58,59]. In this study, both for the whole season and pre-heading stages, most VIs that consisted of the NIR and the red edge bands outperformed the other indices both for AGB (e.g., NDRE, CI_{RE} and DATT) and LAI (e.g., NDRE) estimation, which was consistent with previous studies by Li et al. [58] and Zheng et al. [13]. This might be because the canopy reflectance is largely dominated by canopy-structure-related parameters (e.g., LAI and biomass) during the early growth stages. VIs that consist of the NIR and the red edge bands are also sensitive to the canopy structure and therefore performed better than other models [13,60,61]. However, for post-heading stages, most of the selected VIs were weakly related to the growth parameters, especially for AGB (R^2 < 0.30, RMSE > 3.49 t ha^{-1}). This issue was also encountered in previous studies [14,57] and may be caused by the fact that the NIR and red edge had poor sensitivity to the large biomass during the late stages of crop growth [14,60]. Furthermore, other factors interfered, such as senescent leaves and panicles [57].

Many approaches have been proposed that improve the estimation accuracy for post-heading stages, including the application of three-dimensional information coupled with crop height and hyperspectral information [14] and the combination of texture and spectral information from a UAV image to construct an AGB estimation model [57]. In addition, several studies have also tried to mine information from hyperspectral data: Yao et al. [62] applied continuous wavelet transform to hyperspectral data to improve the estimation accuracy of canopy leaf biomass. However, the models need additional information for these methods and data processing can be tedious and time-consuming (e.g., hyperspectral data). This study applied the LME model to improve the estimation accuracy for post-heading stages. For AGB estimation, the R^2 of the LME model increased by 0.53 compared to SR, while corresponding RMSE values decreased by 1.52 t ha^{-1}. For LAI estimation, the R^2 of LME model increased by 0.23 compared to SR, while corresponding RMSE values decreased by 0.43. The results indicated the LME model as an efficient approach to improve the estimation accuracy for post-heading stages.

4.3. Advantages of the LME Model for Estimating Rice Growth Parameters

As a promising method, the mixed-effect model has been extensively applied for forest remote sensing [31–33]. Compared to other models, the mixed-effect model can better deal with data that are hierarchically structured and grouped [31,32,63]. This model could explain these complex and independent data by breaking down the regression into fixed effects and random effects [49]. The random effects are able to model the deviations from the global relationship within each group [30]. Furthermore, several common types of mixed-effect models exist, including linear mixed-effect (LME) models, generalized linear mixed-effect (GLME) models and non-linear mixed-effect (NLME) models [32,33,64]. Of these types, the LME model is the most popular since it has a better generalization capability; therefore, it was selected for this study [63]. To determine whether the LME model is able to accurately estimate crop growth parameters, the LME model was tested in this study. Furthermore, a comparative analysis of the predictive capability was performed between the LME model and the other three baseline retrieval methods (SR, ANN and RF).

For AGB estimation, the LME model outperformed all other models (SR, ANN and RF) both for the whole season and for different stage groups. For the whole season, a significant improvement was recorded (R^2 = 0.89 and RMSE = 1.75 t ha^{-1}). Compared to the results of coupling crop height with hyperspectral information (R^2 = 0.74 and RMSE = 1.20 t ha^{-1}) by Yue et al. [14] and combining texture and spectral information from UAV images (R^2 = 0.78 and RMSE = 1.84 t ha^{-1}) by Zheng et al. [57], the LME model achieved fairly satisfactory performance. This could be explained by the fact that the growth parameters (AGB or LAI) were not completely independent because the growth parameters might aggregate within different experimental factors (e.g., the random terms in this study: cultivar, planting method and growth stage); thus, these variables were more or less similar. The LME model resolved the data aggregation issue, while traditional retrieval methods did not. Forest research has faced the same challenge because the relationship between volume and biomass with LiDAR metrics differs by stands; therefore, the mixed-effect model is preferable to other models because it addresses the hierarchical nature of forest data by incorporating plot or stand level variability [32]. For each stage group, improvements were moderate for the pre-heading stages (R^2 = 0.86 and RMSE = 1.49 t ha^{-1}) and significant for the post-heading stages (R^2 = 0.75 and RMSE = 1.97 t ha^{-1}). This may be a result of AGB consisting of leaf, stem and panicle biomass after the heading stage. The biomass differences between different organs are more significant, which leads to a more obvious hierarchical nature and aggregation of biological data. This further supports the advantage of the LME model in dealing with hierarchically structured data [63].

With regard to LAI estimation, the ANN and RF regression models showed limited improvements for all stages compared to the SR (whole season: R^2 = 0.66 and RMSE = 1.45; pre-heading stages: R^2 = 0.73 and RMSE = 1.25; post-heading stages: R^2 = 0.53 and RMSE = 1.59). Compared to other models, the LME model achieved a better performance for the whole season (R^2 = 0.79 and RMSE = 1.15) and pre-heading stages (R^2 = 0.81 and RMSE = 1.04) and a significant improvement was recorded found for the post-heading stages (R^2 = 0.76 and RMSE = 1.16). However, the improvements of LAI estimation were not as significant as those of AGB estimation for the post-heading stages. It might be because AGB data aggregation is more palpable than LAI under these random effects. Thus, the LME model was more appropriate for crop AGB estimation.

These results showed that the LME model performs well for rice growth parameters estimation; however, the LME models with different random effects still need to be compared to apply them to practical agricultural production. As shown with the comparison of linear mixed-effect models with different random effects, the combination of cultivar, planting pattern and growth stage performed best (R^2 = 0.89, RMSE = 1.75 t ha^{-1}). However, further analysis suggested that part of the reason for its superiority is that it is segmented into most groups and thus benefits from obtaining the mean of the group. The models that include the random effect of the growth stage also obtained better prediction accuracy compared to other models. Especially, the LME model that uses growth stage as random effect obtained satisfactory estimation accuracy (R^2 = 0.84, RMSE = 2.12 t ha^{-1}), which indicated the growth stage as an important factor for the rice estimation model. In the practical application, the cultivar, planting pattern and growth stage of rice need to be obtained prior to using this model. China established a complete service system for agricultural technology extension and it is easy to obtain crop planting information. For other countries and regions in the world, these data could be collected in different ways. In the USA, crop statistics can be obtained from the Cropland Data Layer (CDL) products, which are produced by the National Agricultural Statistics Service (NASS) of the US Department of Agriculture (USDA) [65]. Furthermore, Farm Service Agency-Common Land Units (FSA-CLU) can also provide such data [66]. In Europe, the data can be generated by the European Union Global Monitoring of Food Security (GMFS) program and JRC's Monitoring Agricultural ResourceS (MARS) action of the European Commission in Ispra (Italy) [67]. In other areas, the crop statistics can be obtained from the Global Information and Early Warning System (GIEWS) of the FAO, which continually receives economic, political and agricultural information from a wide variety of sources (UN organizations, 115 governments, four regional organizations and 61 non-governmental organizations) [66]. Even if the planting information is hard to acquire for a particular region, the rice growth stage can easily be obtained via field observation. In such a case, the LME model, which uses growth stage as random effect, would be a feasible alternative, since the model achieves a sufficient estimation accuracy. The model provides technical support for the building estimation model from field to regional scales in the future.

5. Conclusions

This study explored the potential for the estimation of rice AGB and LAI with a fixed-wing UAV, using the LME model and three baseline retrieval methods (SR, ANN and RF). The results of SR modelling showed that several NIR-based and red edge-based VIs had preferable relationships with growth parameters (AGB and LAI) both for the whole season and pre-heading stages, while all selected VIs were weakly related to growth parameters for post-heading stages. The LME model outperformed the other models (SR, ANN and RF), with the highest R^2 and lowest RMSE for both AGB and LAI estimation. In particular, the LME model significantly improved the estimation accuracy (AGB: $R^2 = 0.75$, RMSE = 1.97 t ha^{-1}; LAI: $R^2 = 0.76$, RMSE = 1.16) for post-heading stages. In summary, this study demonstrates the potential utility of using a fixed-wing UAV combined with the LME model to estimate rice growth parameters. The findings can further serve as a useful reference and technical support for precision farming management and decision-making over large-scale farmland.

Author Contributions: Y.W., K.Z., Q.C. and X.L. conceived and designed the experiments. Y.W., K.Z. and C.T. performed the experiments with support by Y.T., Y.W. and X.L. analyzed the data and wrote the original manuscript, W.C. and Y.Z. provided advice and revised the manuscript. All of the authors have read and approved the final manuscript submitted to the editor.

Funding: The work was funded by the National Key Research and Development Program of China (2016YFD0200602; 2016YFD0300604), the earmarked fund for Jiangsu Agricultural Industry Technology System (JATS(2018)290; JATS(2018)082), the 111 project (B16026) and Jiangsu Province Key Technologies R&D Program (BE2016375).

Acknowledgments: We would like to thank undergraduate student Tai An, Rui Zhang and Ziyi Wang for assistance with field data collection, Wenhui Wang, Xiao Zhang and Penglei Li for their help with sample processing.

Conflicts of Interest: The authors declare no conflict of interest.

References

1. Maimaitijiang, M.; Ghulam, A.; Sidike, P.; Hartling, S.; Maimaitiyiming, M.; Peterson, K.; Shavers, E.; Fishman, J.; Peterson, J.; Kadam, S.; et al. Unmanned Aerial System (UAS)-based phenotyping of soybean using multi-sensor data fusion and extreme learning machine. *ISPRS J. Photogramm. Remote Sens.* **2017**, *134*, 43–58. [CrossRef]
2. Wei, C.; Huang, J.; Mansaray, L.; Li, Z.; Liu, W.; Han, J. Estimation and Mapping of Winter Oilseed Rape LAI from High Spatial Resolution Satellite Data Based on a Hybrid Method. *Remote Sens.* **2017**, *9*, 488. [CrossRef]
3. Ballesteros, R.; Ortega, J.F.; Hernandez, D.; Moreno, M.A. Onion biomass monitoring using UAV-based RGB imaging. *Precis. Agric.* **2018**, *19*, 840–857. [CrossRef]
4. Gao, S.; Niu, Z.; Huang, N.; Hou, X. Estimating the Leaf Area Index, height and biomass of maize using HJ-1 and RADARSAT-2. *Int. J. Appl. Earth. Obs.* **2013**, *24*, 1–8. [CrossRef]
5. Bahn, M.; Rodeghiero, M.; Anderson-Dunn, M.; Dore, S.; Gimeno, C.; Drösler, M.; Williams, M.; Ammann, C.; Berninger, F.; Flechard, C.; et al. Soil Respiration in European Grasslands in Relation to Climate and Assimilate Supply. *Ecosystems* **2008**, *11*, 1352–1367. [CrossRef] [PubMed]
6. Arora, V.K.; Boer, G.J. A parameterization of leaf phenology for the terrestrial ecosystem component of climate models. *Glob. Change Biol.* **2005**, *11*, 39–59. [CrossRef]
7. Drusch, M.; Del Bello, U.; Carlier, S.; Colin, O.; Fernandez, V.; Gascon, F.; Hoersch, B.; Isola, C.; Laberinti, P.; Martimort, P.; et al. Sentinel-2: ESA's Optical High-Resolution Mission for GMES Operational Services. *Remote Sens. Environ.* **2012**, *120*, 25–36. [CrossRef]
8. Yao, Y.; Liu, Q.; Liu, Q.; Li, X. LAI retrieval and uncertainty evaluations for typical row-planted crops at different growth stages. *Remote Sens. Environ.* **2008**, *112*, 94–106. [CrossRef]

9. Duan, T.; Chapman, S.C.; Guo, Y.; Zheng, B. Dynamic monitoring of NDVI in wheat agronomy and breeding trials using an unmanned aerial vehicle. *Field Crop Res.* **2017**, *210*, 71–80. [CrossRef]
10. Yang, G.; Liu, J.; Zhao, C.; Li, Z.; Huang, Y.; Yu, H.; Xu, B.; Yang, X.; Zhu, D.; Zhang, X.; et al. Unmanned Aerial Vehicle Remote Sensing for Field-Based Crop Phenotyping: Current Status and Perspectives. *Front. Plant Sci.* **2017**, *8*, 1111. [CrossRef]
11. Yao, X.; Wang, N.; Liu, Y.; Cheng, T.; Tian, Y.; Chen, Q.; Zhu, Y. Estimation of Wheat LAI at Middle to High Levels Using Unmanned Aerial Vehicle Narrowband Multispectral Imagery. *Remote Sens. Basel* **2017**, *9*, 1304. [CrossRef]
12. Zhang, C.; Kovacs, J.M. The application of small unmanned aerial systems for precision agriculture: A review. *Precis. Agric.* **2012**, *13*, 693–712. [CrossRef]
13. Zheng, H.; Cheng, T.; Li, D.; Yao, X.; Tian, Y.; Cao, W.; Zhu, Y. Combining Unmanned Aerial Vehicle (UAV)-Based Multispectral Imagery and Ground-Based Hyperspectral Data for Plant Nitrogen Concentration Estimation in Rice. *Front. Plant Sci.* **2018**, *9*, 936. [CrossRef] [PubMed]
14. Yue, J.; Yang, G.; Li, C.; Li, Z.; Wang, Y.; Feng, H.; Xu, B. Estimation of Winter Wheat Above-Ground Biomass Using Unmanned Aerial Vehicle-Based Snapshot Hyperspectral Sensor and Crop Height Improved Models. *Remote Sens. Basel* **2017**, *9*, 708. [CrossRef]
15. Devia, C.A.; Rojas, J.P.; Petro, E.; Martinez, C.; Mondragon, I.F.; Patino, D.; Rebolledo, M.C.; Colorado, J. High-Throughput Biomass Estimation in Rice Crops Using UAV Multispectral Imagery. *J. Intell. Robot Syst.* **2019**, 1–17. [CrossRef]
16. Duan, B.; Fang, S.; Zhu, R.; Wu, X.; Wang, S.; Gong, Y.; Peng, Y. Remote Estimation of Rice Yield with Unmanned Aerial Vehicle (UAV) Data and Spectral Mixture Analysis. *Front. Plant Sci.* **2019**, *10*, 204. [CrossRef] [PubMed]
17. Sankaran, S.; Khot, L.R.; Espinoza, C.Z.; Jarolmasjed, S.; Sathuvalli, V.R.; Vandemark, G.J.; Miklas, P.N.; Carter, A.H.; Pumphrey, M.O.; Knowles, N.R.; et al. Low-altitude, high-resolution aerial imaging systems for row and field crop phenotyping: A review. *Eur. J. Agron.* **2015**, *70*, 112–123. [CrossRef]
18. Yang, S.; Feng, Q.; Liang, T.; Liu, B.; Zhang, W.; Xie, H. Modeling grassland above-ground biomass based on artificial neural network and remote sensing in the Three-River Headwaters Region. *Remote Sens. Environ.* **2018**, *204*, 448–455. [CrossRef]
19. Yuan, H.; Yang, G.; Li, C.; Wang, Y.; Liu, J.; Yu, H.; Feng, H.; Xu, B.; Zhao, X.; Yang, X. Retrieving Soybean Leaf Area Index from Unmanned Aerial Vehicle Hyperspectral Remote Sensing: Analysis of RF, ANN and SVM Regression Models. *Remote Sens. Basel* **2017**, *9*, 309. [CrossRef]
20. Wang, L.; Zhou, X.; Zhu, X.; Dong, Z.; Guo, W. Estimation of biomass in wheat using random forest regression algorithm and remote sensing data. *Crop J.* **2016**, *4*, 212–219. [CrossRef]
21. Li, H.; Chen, Z.; Jiang, Z.; Wu, W.; Ren, J.; Liu, B.; Tuya, H. Comparative analysis of GF-1, HJ-1 and Landsat-8 data for estimating the leaf area index of winter wheat. *J. Integr. Agric.* **2017**, *16*, 266–285. [CrossRef]
22. Huang, Z.; Turner, B.J.; Dury, S.J.; Wallis, I.R.; Foley, W.J. Estimating foliage nitrogen concentration from HYMAP data using continuum removal analysis. *Remote Sens. Environ.* **2004**, *93*, 18–29. [CrossRef]
23. Shen, W.; Li, M.; Huang, C.; Tao, X.; Wei, A. Annual forest aboveground biomass changes mapped using ICESat/GLAS measurements, historical inventory data and time-series optical and radar imagery for Guangdong province, China. *Agric. For. Meteorol.* **2018**, *259*, 23–38. [CrossRef]
24. Li, Z.; Wang, J.; Tang, H.; Huang, C.; Yang, F.; Chen, B.; Wang, X.; Xin, X.; Ge, Y. Predicting Grassland Leaf Area Index in the Meadow Steppes of Northern China: A Comparative Study of Regression Approaches and Hybrid Geostatistical Methods. *Remote Sens. Basel* **2016**, *8*, 632. [CrossRef]
25. Näsi, R.; Viljanen, N.; Kaivosoja, J.; Alhonoja, K.; Hakala, T.; Markelin, L.; Honkavaara, E. Estimating Biomass and Nitrogen Amount of Barley and Grass Using UAV and Aircraft Based Spectral and Photogrammetric 3D Features. *Remote Sens. Basel* **2018**, *10*, 1082.
26. Corti, M.; Cavalli, D.; Cabassi, G.; Marino Gallina, P.; Bechini, L. Does remote and proximal optical sensing successfully estimate maize variables? A review. *Eur. J. Agron.* **2018**, *99*, 37–50. [CrossRef]
27. Kang, Y.; Özdoğan, M.; Zipper, S.; Román, M.; Walker, J.; Hong, S.; Marshall, M.; Magliulo, V.; Moreno, J.; Alonso, L.; et al. How Universal Is the Relationship between Remotely Sensed Vegetation Indices and Crop Leaf Area Index? A Global Assessment. *Remote Sens. Basel* **2016**, *8*, 597. [CrossRef]
28. Tremblay, N.; Wang, Z.; Ma, B.; Belec, C.; Vigneault, P. A comparison of crop data measured by two commercial sensors for variable-rate nitrogen application. *Precis. Agric.* **2009**, *10*, 145–161. [CrossRef]

29. Shaver, T.M.; Khosla, R.; Westfall, D.G. Evaluation of two crop canopy sensors for nitrogen variability determination in irrigated maize. *Precis. Agric.* **2011**, *12*, 892–904. [CrossRef]
30. Pinheiro, J.; Bates, D. *Mixed-Effects Models in S and S-PLUS*; Springer Science & Business Media: Berlin/Heidelberg, Germany, 2006.
31. Zuur, A.F.; Ieno, E.N.; Walker, N.J.; Saveliev, A.A.; Smith, G.M. *Mixed Effects Models and Extensions in Ecology with R*; Springer: New York, NY, USA, 2009.
32. Poudel, K.; Flewelling, J.; Temesgen, H. Predicting Volume and Biomass Change from Multi-Temporal Lidar Sampling and Remeasured Field Inventory Data in Panther Creek Watershed, Oregon, USA. *Forests* **2018**, *9*, 28. [CrossRef]
33. Chen, D.; Huang, X.; Zhang, S.; Sun, X. Biomass Modeling of Larch (Larix spp.) Plantations in China Based on the Mixed Model, Dummy Variable Model and Bayesian Hierarchical Model. *Forests* **2017**, *8*, 268. [CrossRef]
34. Liu, X.; Cao, Q.; Yuan, Z.; Liu, X.; Wang, X.; Tian, Y.; Cao, W.; Zhu, Y. Leaf area index based nitrogen diagnosis in irrigated lowland rice. *J. Integr. Agric.* **2018**, *17*, 111–121. [CrossRef]
35. Zhang, K.; Ge, X.; Shen, P.; Li, W.; Liu, X.; Cao, Q.; Zhu, Y.; Cao, W.; Tian, Y. Predicting Rice Grain Yield Based on Dynamic Changes in Vegetation Indexes during Early to Mid-Growth Stages. *Remote Sens. Basel* **2019**, *11*, 387. [CrossRef]
36. Chianucci, F.; Disperati, L.; Guzzi, D.; Bianchini, D.; Nardino, V.; Lastri, C.; Rindinella, A.; Corona, P. Estimation of canopy attributes in beech forests using true colour digital images from a small fixed-wing UAV. *Int. J. Appl. Earth Obs.* **2016**, *47*, 60–68. [CrossRef]
37. Han, L.; Yang, G.; Dai, H.; Xu, B.; Yang, H.; Feng, H.; Li, Z.; Yang, X. Modeling maize above-ground biomass based on machine learning approaches using UAV remote-sensing data. *Plant Methods* **2019**, *15*, 10. [CrossRef] [PubMed]
38. Hassan, M.; Yang, M.; Rasheed, A.; Jin, X.; Xia, X.; Xiao, Y.; He, Z. Time-Series Multispectral Indices from Unmanned Aerial Vehicle Imagery Reveal Senescence Rate in Bread Wheat. *Remote Sens. Basel* **2018**, *10*, 809. [CrossRef]
39. Rouse, J.W.; Haas, R.H.; Schell, J.A.; Deering, D.W. Monitoring vegetation systems in the great plains with ERTS. In *Third Earth Resources Technology Satellite-1 Symposium-Volume I: Technical Presentation*; NASA SP-351; NASA: Washington, DC, USA, 1974.
40. Gitelson, A.; Merzlyak, M.N. Quantitative estimation of chlorophyll-a using reflectance spectra: Experiments with autumn chestnut and maple leaves. *J. Photochem. Photobiol. B Biol.* **1994**, *22*, 247–252. [CrossRef]
41. Gitelson, A.A. Remote estimation of canopy chlorophyll content in crops. *Geophys. Res. Lett.* **2005**, *32*, 1–4. [CrossRef]
42. Qi, J.; Chehbouni, A.; Huete, A.R.; Kerr, Y.H.; Sorooshian, S.S. A modified soil adjusted vegetation index. *Remote Sens. Environ.* **1994**, *48*, 119–126. [CrossRef]
43. Rondeaux, G.; Steven, M.; Baret, F. Optimization of soil-adjusted vegetation indices. *Remote Sens. Environ.* **1996**, *55*, 95–107. [CrossRef]
44. Sankaran, S.; Mishra, A.; Ehsani, R.; Davis, C. A review of advanced techniques for detecting plant diseases. *Comput. Electron. Agric.* **2010**, *72*, 1–13. [CrossRef]
45. Haboudane, D. Hyperspectral vegetation indices and novel algorithms for predicting green LAI of crop canopies: Modeling and validation in the context of precision agriculture. *Remote Sens. Environ.* **2004**, *90*, 337–352. [CrossRef]
46. Datt, B. Visible/near infrared reflectance and chlorophyll content in Eucalyptus leaves. *INT J. Remote Sens.* **2010**, *20*, 2741–2759. [CrossRef]
47. Gitelson, A.A.; Kaufman, Y.J.; Merzlyak, M.N. Use of a green channel in remote sensing of global vegetation from EOS-MODIS. *Remote Sens. Environ.* **1996**, *58*, 289–298. [CrossRef]
48. Breiman, L. Random forests. *Mach. Learn.* **2001**, *45*, 5–32. [CrossRef]
49. Bennington, C.C.; Thayne, W.V. Use and Misuse of Mixed Model Analysis of Variance in Ecological Studies. *Ecology* **1994**, *75*, 717–722. [CrossRef]
50. Pollice, A.; Bilancia, M. Kriging with mixed effects models. *Statistica* **2002**, *62*, 405–429.
51. Cressie, N. Statistics for spatial data. *Terra Nova* **1992**, *4*, 613–617. [CrossRef]
52. Liu, H.J.; Zheng, J.C.; Chen, L.G.; Zhou, W. Effects of different planting modes on the growth and development characteristics of rice. *Chin. J. Ecol.* **2013**, *32*, 2326–2331.

53. Yan, D.; Zhu, Y.; Wang, S.; Cao, W. A quantitative knowledge-based model for designing suitable growth dynamics in rice. *Plant Prod. Sci.* **2006**, *9*, 93–105. [CrossRef]
54. Zhang, C.; Walters, D.; Kovacs, J.M. Applications of Low Altitude Remote Sensing in Agriculture upon Farmers' Requests—A Case Study in Northeastern Ontario, Canada. *PLoS ONE* **2014**, *9*, e112894. [CrossRef] [PubMed]
55. Zarco-Tejada, P.J.; Diaz-Varela, R.; Angileri, V.; Loudjani, P. Tree height quantification using very high resolution imagery acquired from an unmanned aerial vehicle (UAV) and automatic 3D photo-reconstruction methods. *Eur. J. Agron.* **2014**, *55*, 89–99. [CrossRef]
56. Vivoni, E.R.; Rango, A.; Anderson, C.A.; Pierini, N.A.; Schreiner-McGraw, A.P.; Saripalli, S.; Laliberte, A.S. Ecohydrology with unmanned aerial vehicles. *Ecosphere* **2014**, *5*, 1–14. [CrossRef]
57. Zheng, H.; Cheng, T.; Zhou, M.; Li, D.; Yao, X.; Tian, Y.; Cao, W.; Zhu, Y. Improved estimation of rice aboveground biomass combining textural and spectral analysis of UAV imagery. *Precis. Agric.* **2018**, 1–19. [CrossRef]
58. Li, S.; Ding, X.; Kuang, Q.; Ata-UI-Karim, S.T.; Cheng, T.; Liu, X.; Tian, Y.; Zhu, Y.; Cao, W.; Cao, Q. Potential of UAV-Based Active Sensing for Monitoring Rice Leaf Nitrogen Status. *Front. Plant Sci.* **2018**, *9*, 1834. [CrossRef] [PubMed]
59. Liu, X.; Ferguson, R.; Zheng, H.; Cao, Q.; Tian, Y.; Cao, W.; Zhu, Y. Using an Active-Optical Sensor to Develop an Optimal NDVI Dynamic Model for High-Yield Rice Production (Yangtze, China). *Sensors Basel* **2017**, *17*, 672. [CrossRef]
60. Cheng, T.; Song, R.; Li, D.; Zhou, K.; Zheng, H.; Yao, X.; Tian, Y.; Cao, W.; Zhu, Y. Spectroscopic Estimation of Biomass in Canopy Components of Paddy Rice Using Dry Matter and Chlorophyll Indices. *Remote Sens. Basel* **2017**, *9*, 319. [CrossRef]
61. Knipling, E.B. Physical and physiological basis for the reflectance of visible and near-infrared radiation from vegetation. *Remote Sens. Environ.* **1970**, *1*, 155–159. [CrossRef]
62. Yao, X.; Si, H.; Cheng, T.; Jia, M.; Chen, Q.; Tian, Y.; Zhu, Y.; Cao, W.; Chen, C.; Cai, J.; et al. Hyperspectral Estimation of Canopy Leaf Biomass Phenotype per Ground Area Using a Continuous Wavelet Analysis in Wheat. *Front. Plant Sci.* **2018**, *9*, 1360. [CrossRef]
63. Goldstein, H. *Multilevel Statistical Models*; John Wiley & Sons: Hoboken, NJ, USA, 2011.
64. Rigling, A.; Bigler, C.; Eilmann, B.; Feldmeyer-Christe, E.; Gimmi, U.; Ginzler, C. Driving factors of a vegetation shift from Scots pine to pubescent oak in dry Alpine forests. *Glob. Change Biol.* **2013**, *19*, 229–240. [CrossRef]
65. Boryan, C.; Yang, Z.; Mueller, R.; Craig, M. Monitoring US agriculture: the US Department of Agriculture, National Agricultural Statistics Service, Cropland Data Layer Program. *Geocarto Int.* **2011**, *26*, 341–358. [CrossRef]
66. Gallego, J.; Carfagna, E.; Baruth, B. Accuracy, objectivity and efficiency of remote sensing for agricultural statistics. In *Agricultural Survey Methods*; John Wiley & Sons, Ltd.: Hoboken, NJ, USA, 2010; pp. 193–211.
67. Atzberger, C. Advances in remote sensing of agriculture: Context description, existing operational monitoring systems and major information needs. *Remote Sens. Basel* **2013**, *5*, 949–981. [CrossRef]